Automated Crater Detection, A New Tool for Mars Cartography and Chronology

Jung Rack Kim, Jan-Peter Muller, Stephan van Gasselt, Jeremy G Morley, Gerhard Neukum, and the HRSC CoI Team

Abstract

An automated crater detection algorithm is presented which exploits image data. The algorithm is briefly described and its application demonstrated on a variety of different Martian geomorphological areas and sensors (Viking Orbiter Camera, Mars Orbiter Camera (MOC), Mars Orbiter Laser Altimeter (MOLA), and High Resolution Stereo Camera (HRSC)). We show assessment results through both an inter-comparison of automated crater locations with those from the manually-derived Mars Crater Consortium (MCC) catalogue and the manually-derived craters. The detection algorithm attains an accuracy of 70 to 90 percent and a quality factor of 60 to 80 percent depending on target sensor type and geomorphology. We also present crater detection results derived from HRSC images onboard the ESA Mars Express on a comparison between manually-determined Size-Frequency Distributions (SFDs) and those derived fully automatically. The approach described appears to offer great potential for chronological research, geomatic and geological analysis and for other purposes of extra-terrestrial planetary surface mapping.

Introduction

Purpose

Impact craters are key geomorphological structures formed by the collision of a meteoroid, asteroid or comet with a planetary surface. Their measurement, detection and derived crater size frequency distribution (SFDs) have a very high priority for Extra Terrestrial Mapping due to their importance in being the only remotely sensed method generally applicable for surface aging. In spite of the increasing demand over the last few decades for automated geomorphometric tools from the geological community and their importance in geodetic control, the application of machine vision to detect automatically impact craters does not appear to have been very successful or was only successful in extremely limited domains such as their use in autonomous landing on extra-terrestrial bodies. The main reasons for this, we believe, can be summarized as follows:

1. The "visibility" of impact craters in optical images depends principally on the interaction between the illumination and incidence (view) direction, surface scattering behavior and the atmospheric state (which is particularly important for Mars).

2. Some geographical features such as small volcanic constructs or valleys have similar morphological characteristics as craters.
3. Impact craters are often concentrated into clusters resulting in overlap, and in larger craters multi-ring structures frequently occur. This means that the separation of individual craters from their background can be very difficult to generalize.
4. Crater rims on Mars are frequently eroded due to surface processes such as wind, as discussed by Kuzmin *et al.* (2001), as well as increasingly recognized, the action of water, which has been studied by Forsberg-Taylor *et al.* (2004).
5. Except for MOLA data which are relevant only to very large impact crater structures, sufficiently accurate and complete 3D data has not previously been available to allow automated detection using either 3D (DTM) data alone or fused with image data (see later).

To address these problems, a combinatorial data fusion technique based on machine vision algorithms has been developed. Here we report on an evaluation of the crater detected products with manually detected craters and the MCC catalogue (Barlow *et al.*, 2002) and show a practical application to the age determination of the Martian surface.

Previous Research Work

Several methods to detect craters automatically have been developed but do not yet appear to be ready for operational use. One of the first feature recognition systems for impact crater detection on Mars was proposed by Vinogradova *et al.* (2002). Another approach for small craters on an asteroid, which appears to be relatively successful, is the work of Leroy *et al.* (2001). The primary aim of their research was the automated detection of impact craters and the 3D modeling of asteroids. Honda *et al.* (2002) developed a planetary topographic feature mining system for the extraction of lunar craters. One interesting point of their research was the introduction of a false alarm exclusion algorithm using a technique called a Self-Organizing Map (SOM), which is somewhat similar to the false detection removal method described here. However, they reported that the detection rate achieved with their approach was not useful for scientific analysis.

Cheng *et al.* (2003) developed a crater detection algorithm and applied it to automated navigation over extra-terrestrial small bodies. Magee *et al.* (2003) showed results from an automated impact crater detection by edge processing and template matching. Kim and Muller (2003)

Jung Rack Kim, Jan-Peter Muller, and Jeremy G. Morley are with the Department of Geomatic Engineering, University College London, Gower Street, London, WC1E 6BT UK (jkim@ge.ucl.ac.uk).

Stephan van Gasselt and Gerhard Neukum are with the Freie Universität Berlin, Institute of Geological Sciences, Remote Sensing of the Earth and Planets, Malteserstr. 74-100, D-12249 Berlin, Germany.

suggested a similar crater detection method, but employing texture analysis and ellipse fitting on the DTM and optical image. A search of the non-refereed literature shows there are a number of techniques being developed but no quantitative information on their accuracy, reliability, or completeness is reported.

Algorithms

The overall procedure consists of three stages First (see Figure 1), a *focusing stage* defines target edge segments in so-called Regions of Interest (ROIs). These "preliminary crater edges" are then organized to locate optimal ellipses in a second processing step. Optimal circles, or ellipses (due to the perspective distortion of spacecraft images) for impact craters are then evaluated using a fitness function and refined and verified by template matching. Finally, false alarms (false detections) are removed using a neural network-based false crater recognition scheme.

In the following sub-sections, further details, albeit limited by space, are provided of these individual stages.

Focusing

When applying the first stage, there are usually too many connected edge segments in an optical image. A focusing strategy using a texture classification and edge direction analysis is therefore used here to reduce the search space. Grey level co-occurrence matrices (GLCMs) (Haralick, 1979) are widely used to extract texture properties, and these texture properties can be simply classified using a *k*-means

Figure 1. Schematic diagram of overall work flow and processing steps for the Kim-Muller (KM) automated crater detection system.

clustering into a ROI. The texture properties of GLCMs which are employed in this work were moments, contrast, and homogeneity using a window of 5 to 12 pixel size depending on the minimum size of the desired target crater. The ROIs of contiguous craters frequently overlap so that a splitting process based on a simple morphological distance transformation was applied as follows:

$$D_x(p) = \min_{x \in R}\|p - X\|$$
$$s - [X^t : D_X(p) < d_{\max}]$$
$$R\_R = (S \oplus s)_i = (S \oplus s) \otimes \cdots \oplus s \quad (1)$$

where D_X is the Euclidean distance transformation of point X from the nearest boundary p, s is the structuring element of a morphological filter, usually of size 3 pixels by 3 pixels, X' are all points within distance $d_{\max}$ from the nearest boundary, where $d_{\max}$ are decided by the size of GLCM window, S is the skeleton by the distance transformation, $\oplus_i$ is the ith application of a binary dilation where the number of dilations i depend on the value of $d_{\max}$, and R_R is the reconstructed ROI.

In this equation, we employed an Euclidean distance transformation using grayscale morphology (Huang and Mitchell, 1994) to split attached ROIs during the texture classification stage, which are then reconstructed into their original shape by recursive binary dilation.

Here, an edge is localized by its ROI, which is defined through a GLCM texture classification. This GLCM-based texture analysis is applied iteratively to some ROIs, which are larger than a predefined critical size, as these could be candidates for composite craters (Figure 2b).

Edge thresholding was performed by the following procedures within a localized edge area. As shown in Figure 3, which shows a simulated crater image derived from a generalized 3D crater model using a Phong surface shading model, there are four edge segments: *Seg1*, *Seg2*, *Seg3*, and *Seg4*. The real crater rim edge is usually defined as the boundary between the illuminated and shadowed areas, such as *Seg1* and *Seg2*. An evaluation of the edges in the four detected regions based on this criterion can be made by looking at the maxima (M_x1, M_x2 in Figure 3b) of the crater edge segments and the extent of the crater edge rim.

As is typical, the edge magnitude and direction can be defined as:

$$I_e = sqrt(G_x^2 + G_y^2)$$
$$\varphi = \arctan(\frac{G_y}{G_x}) \quad (2)$$

where Gx is the x gradient of intensity, and Gy is the y gradient of intensity.

Here, the maxima refer to the points where the angles between solar illumination and an edge direction are perpendicular as shown in Figure 3a, and consequently, the edge magnitudes (I_e) are at a maximum in each edge segment (Figure 3b).

The extent of a crater edge can usually be defined by the edge direction range $\pm90°$ from maxima. Therefore, the edge lines in the crater rim parts can be traced and extracted by employing the following method. An initial estimation of the radius, r, can be replaced by a mean dimension of ROI (r_i) using a moment analysis as follows

$$r_i = (L_{major} + L_{\min or})/2.0$$
$$L_{major} = \sqrt{\frac{12M_{20}}{M_{00}}}, L_{\min or} = \sqrt{\frac{12M_{02}}{M_{00}}}$$
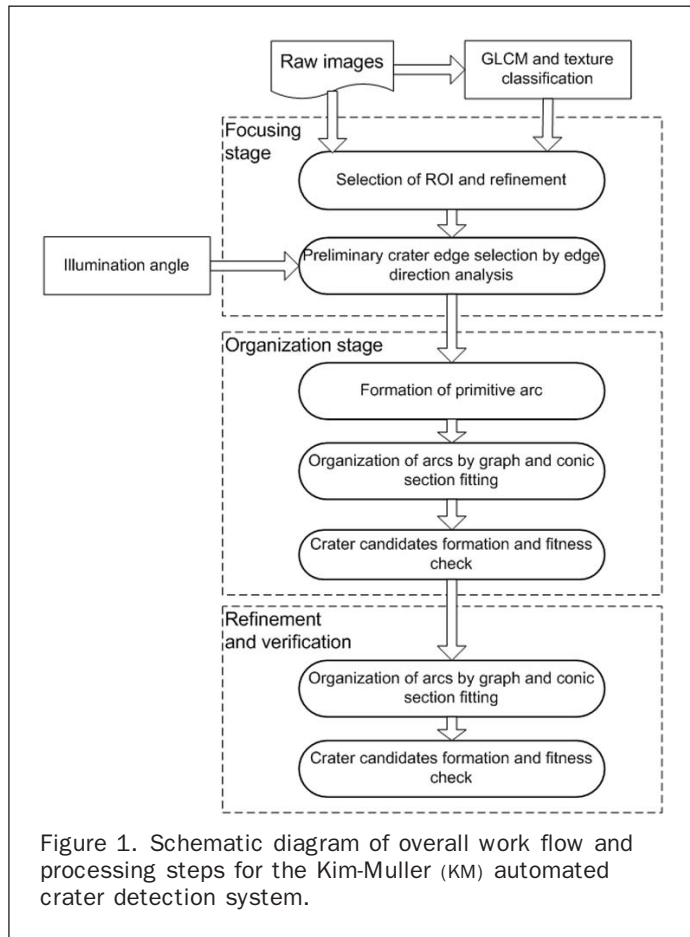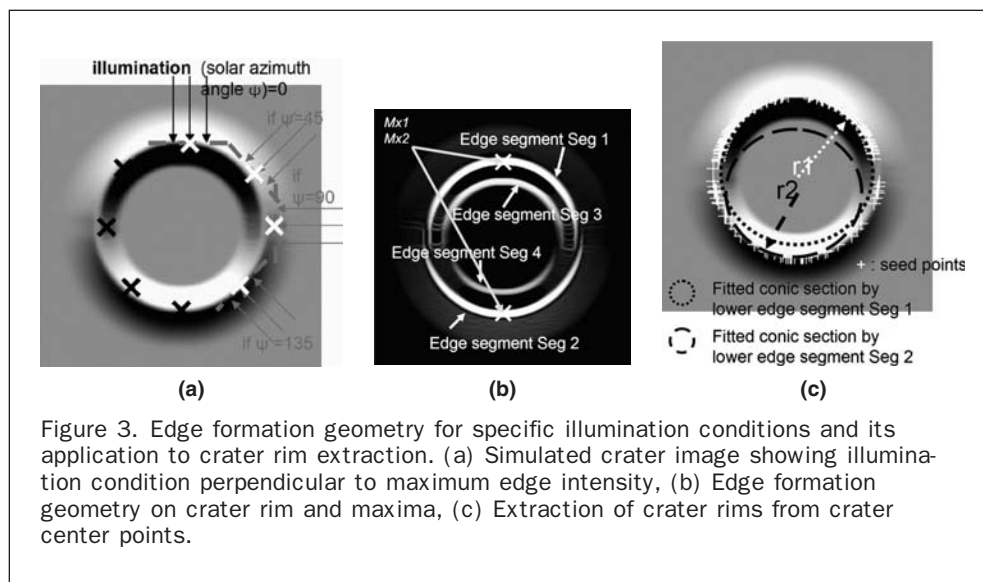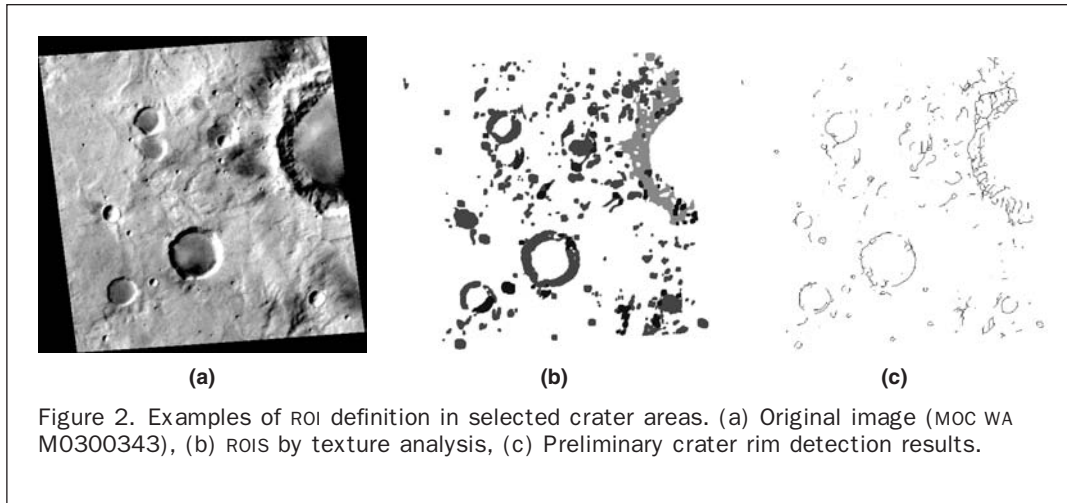$$M_{ij} = \sum_{x_k \in R}\sum_{y_k \in R} x_k^i y_k^i \quad (3)$$

Figure 2. Examples of ROI definition in selected crater areas. (a) Original image (MOC WA M0300343), (b) ROIS by texture analysis, (c) Preliminary crater rim detection results.

Figure 3. Edge formation geometry for specific illumination conditions and its application to crater rim extraction. (a) Simulated crater image showing illumination condition perpendicular to maximum edge intensity, (b) Edge formation geometry on crater rim and maxima, (c) Extraction of crater rims from crater center points.

For all of the edge pixels with r which are estimated from (Equation 3) in the φ (edge direction) space, the maximum edge intensity point in each $\Delta\varphi$ interval is detected from the edge direction of the maxima to $\pm 90°$. This procedure can be used to detect "seed points" (see Figure 3c). By applying region growing to these seed points using a four-way connectivity within a fixed edge magnitude, the extent of the preliminary crater rim edges can be precisely defined as illustrated in Figure 2c. See Kim *et al.* (2004) for several examples of the robustness of this algorithm with a large range of different illumination angles.

Edge Organization
The preliminary crater rims are defined in the first focusing stage. However the edges of the preliminary crater rims need to be organized into generalized shapes, particularly optimal ellipses or circles from the input arbitrary edge lines so that consequent verification stages using the parameters of the conic sections (i.e., radius and center point) can be easily applied.

Impact craters on geometrically corrected images of planetary surfaces are generally circular features, so that the eccentricity in any target image is calculable given the image acquisition geometry. Exceptional cases are (a) Rare elliptical impact craters (eccentricity >1.1) are produced when the impact angles are low relative to the horizontal. These elliptical impact craters form approximately 5 percent of all kilometer sized craters formed on Mars, Venus, and the Moon (Bottke *et al.*, 2000); (b) The foreshortening of a circle into an ellipse by the oblique view from a framing camera (Viking imagery) or by non-optimal choice of interline time in a pushbroom sensor; and (c) More complex distortions which can be produced through the uneven motion of a pushbroom sensor (e.g., as described for the MOC Narrow Angle camera by Kirk *et al.*, 2003), resulting in slightly non-elliptical shapes. However, it should be noted that the majority of such distorted craters can be suitably modeled as conic sections with a marginal eccentricity value. In case (b) the orientation and eccentricity are known *a priori*.

The most widely applied edge organization method for circle or ellipse detection is the Hough transformation. There are a number of modified versions for efficient detection of ellipses or circles such as those proposed by Yuen *et al.* (1989) and Olson (1998). However, from our experience, none of these methods appear to be sufficiently robust to guarantee the reliable detection of impact craters from a set of preliminary crater rim edges. Hence, we addressed this
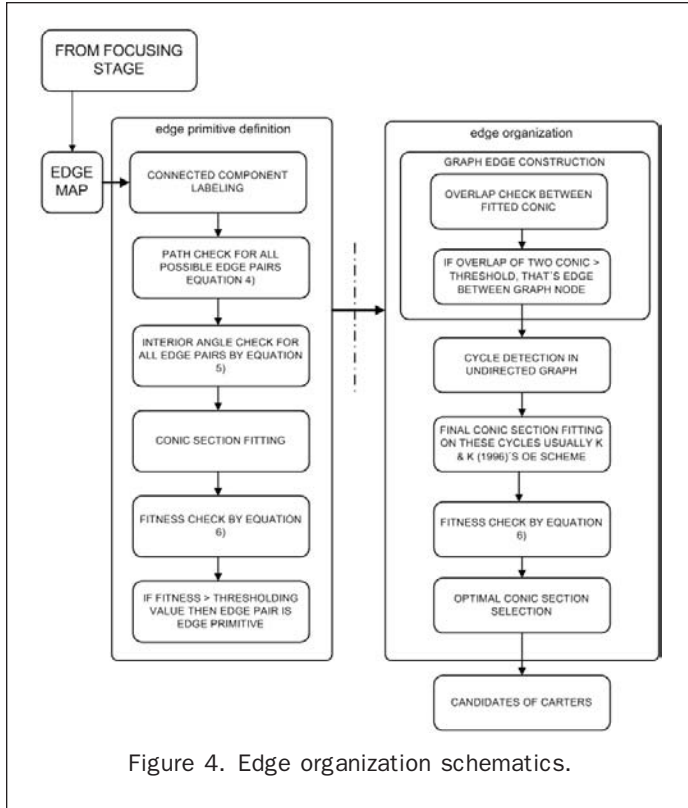
Figure 4. Edge organization schematics.

Figure 5. Schematic diagram showing the geometry of the intersection angle (θ_{in}) of edge i,j (a) and the fitness function (b):

fitted conic section, are satisfied, then an edge pair, $e(i,j)$, is deemed to form an "edge primitive"

$$Ecc_{e(i,j)} < Ecc_{th}$$
$$Fit_{e(i,j)} > Fit_{th}$$

$$Fit_{e(i,j)} = \sum_x \sum_y (T(x,y) \cap B(x,y)) / \sum_x \sum_y B(x,y)$$
$$B(x,y) = b(x,y) \oplus s \qquad (6)$$

where $Ecc_{e(i,j)}$ is the eccentricity of edge pair $e(i,j)$, Ecc_{th} and Fit_{th} are threshold values of eccentricity and fitness, $T(x,y)$ is the thresholded edge image which was processed from the previous crater rim extraction process, $b(x,y)$ is the binary image of the fitted conic section, and s is the structuring element of binary dilation at size n_s, which itself depends on the radius (r) of the fitted conic section, usually $0.1r$ to $0.2r$ in pixels.

After selection from several conic section fitting methods, two algorithms were principally employed in our work. One is the Direct Least Squared (DLS) fitting method (Fitzgibbon *et al.*, 1999), and the other uses conic fitting by optimal estimation (OE) (Kanazawa and Kanantani, 1996). A detailed description of these algorithms is beyond the scope of this article; interested readers are advised to consult the above references. Both algorithms appear to be reliable even with quite noisy data, with the OE fitting scheme showing the highest accuracy with relatively short arcs, as are frequently observed in Martian crater rims. However, the CPU cost of the OE covariance tensor approach and iterative renormalization is more expensive compared with the DLS fitting scheme. Therefore, the DLS fitting scheme was employed in edge organization as the default method. In the final fitting stage to find the best conic section from different crater candidates, OE is used. If both methods fail, the circle fitting method of Thomas and Chan (1989), which is based on a regression formula to extract the circle radius and the center point from irregularly spaced points, is employed with the assumption that the image is already adjusted for foreshortening or non-unity aspect ratio through geometric correction.

All edge primitives are formed from the potential edge pairs $e(i,j)$ and edge arcs, which are also verified by the fitness ratio in Equation 6. Then, the edge primitives are used to form the nodes of a graph and all the possible edge primitives between graph nodes are checked. At all graph nodes, conic sections are fitted once more and the intersection ratios of the fitted circles or ellipses and fitness are examined to identify graph edges by these two conditions:

$$\frac{En(i) \cap En(j)}{En(i) \cup En(j)} > Op_{th} \qquad (7)$$
$$Fit_{e(i,j)} > Fit_{th}$$

problem using conic section fitting and graph based edge organization as shown schematically in Figure 4.

The edge organization stage is a consecutive evolution process. Starting from crater rim edges, edge pairs are then formed into edge primitives which are then verified from edge pairs or edge arcs (single edge sets) to form a set of graph nodes. Finally conic sections are fitted to the cycles of these edge primitive nodes within the graph.

First, a possible edge pair map is constructed using the following conditions:

$$Max(S_{ix}, S_{iy}) + Max(S_{jx}, S_{jy}) < \|Ce_i - Ce_j\| \qquad (4)$$

where (S_{ix}, S_{iy}) and (S_{jx}, S_{jy}) are the geometrical x, y dimensions of edge segment i, j, and Ce_i, Ce_j are the center locations of edge segments i, j. Equation 4 means that an edge pair is accepted if the sum of its geometrical dimension is smaller than the distance between center points. If an edge pair $e(i,j)$ is possible through condition (Equation 4), the interior angle, θ_{in} of that edge pair is checked as follows (see Figure 5a; Kim and Kim, 2001).

$$\theta_{in} < \theta_t$$
$$\theta_{in} = \cos^{-1}\left(\frac{\overrightarrow{IM(i)} \cdot \overrightarrow{IM(j)}}{|\overrightarrow{IM(i)}| \cdot |\overrightarrow{IM(j)}|}\right) \qquad (5)$$

where $IM(i), IM(j)$ are the vectors of the intersection point I of edge pair $e(i, j)$, and mid-point of edge i, j and θ_t is the threshold value for the interior angle, usually taken as 135°.

A fitness function, conceptually illustrated in Figure 5b is introduced to evaluate the ratio of target edge points which is covered by a fitted conic section. An eccentricity check is then used to assess the reliability of the fitted ellipse. This consists of a process to construct a node of the edge graph in the organization step. If the following two conditions, known as the *eccentricity constraint* and the *fitness constraint* for the
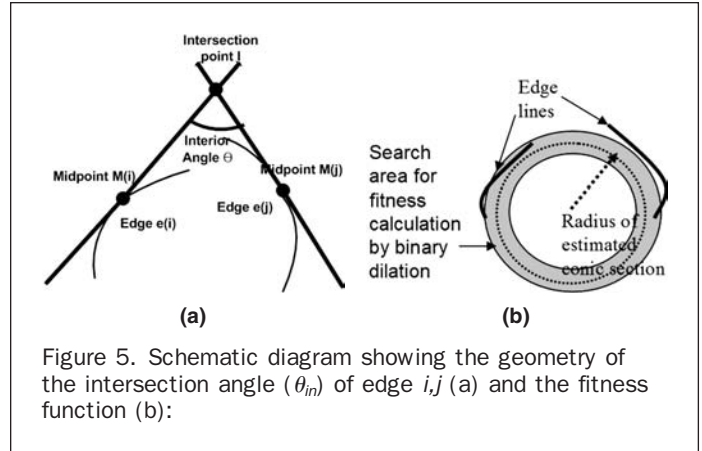
where *En(i)* are the enclosed parts by node *i*, *En(j)* are the enclosed parts by node *j*, Op_{th} is the threshold overlap value (usually 0.5), and Fit_{th} is the thresholded value of fitness, usually taken as 0.3.

If both conditions are satisfied, the edges between nodes are connected, so that they form a unidirectional graph. Then, all possible cycles are detected as shown schematically in Figure 6c. Among all of these possible cycles, the best-matched cycle is selected by the chosen conic section fitting process and fitness function. Then, the longest nodes of that cycle are removed from other cycles. This is an iterative process based on the hypothesis that the longest edge of any impact crater should not be shared by any other impact craters, such that a repeat detection of the same crater by another graph cycle is prevented. From this we obtain the best-fit conic section for all edges and combination of edges (see examples in Figure 6d and e).

Refinement and Verification

To assess the preliminary ellipses, conic sections are again fitted to the edge points of each ellipse by optimal estimation, and the fitness is evaluated once more for each ellipse. If the fitness value is higher than a pre-specified threshold value (usually 0.4), the ellipse is considered as a potential crater boundary. This additional refinement step is necessary because as seen in Figure 7a, the outlines of the crater rims are sometimes not correctly matched with the finally fitted ellipse. The final verification stage uses template matching at several fixed radii and center point ranges with different margins. It is also considered here as an internal verification stage. As we already have estimated

the approximate size of the detected crater candidates through the previous edge organization stage, it is possible to examine the correlation value between a predefined template and the detected crater candidates. First, the predefined synthetic crater images are selected for the relevant illumination conditions (sun azimuth angle is used here) as the detected crater candidate image. Then around the center of the crater candidates, which we refer to as the *core* (Figure 7b), templates of different sizes are applied and correlation values with the target image patch, are checked. This could be a very time consuming process, however, as we already know the approximate radius and center of the target crater, unacceptable CPU times for this stage are avoided.

From the correlation values resulting from the applied templates, a maximum value is chosen for each crater candidate. If this value is higher than some predefined threshold value ($Corr_{th} = 0.6$ usually), the verification process is deemed successful. Then, the template size and center of the correlation are extracted which yields more accurate crater center locations and corresponding radii (Figure 7c).

However, for some craters, where the target crater has some irregular features such as a flat-bed floor or eroded rim, the template based verification is not suitable because the correlation value is too low. In such cases, the candidate crater rim edge would not be correctly defined, and exact resizing and location of center points is not feasible. In such cases, the Gruen (1985) image matching scheme, which has been shown by many authors to be the best solution for the registration between distorted image patches, is introduced to address geometrical distortions instead
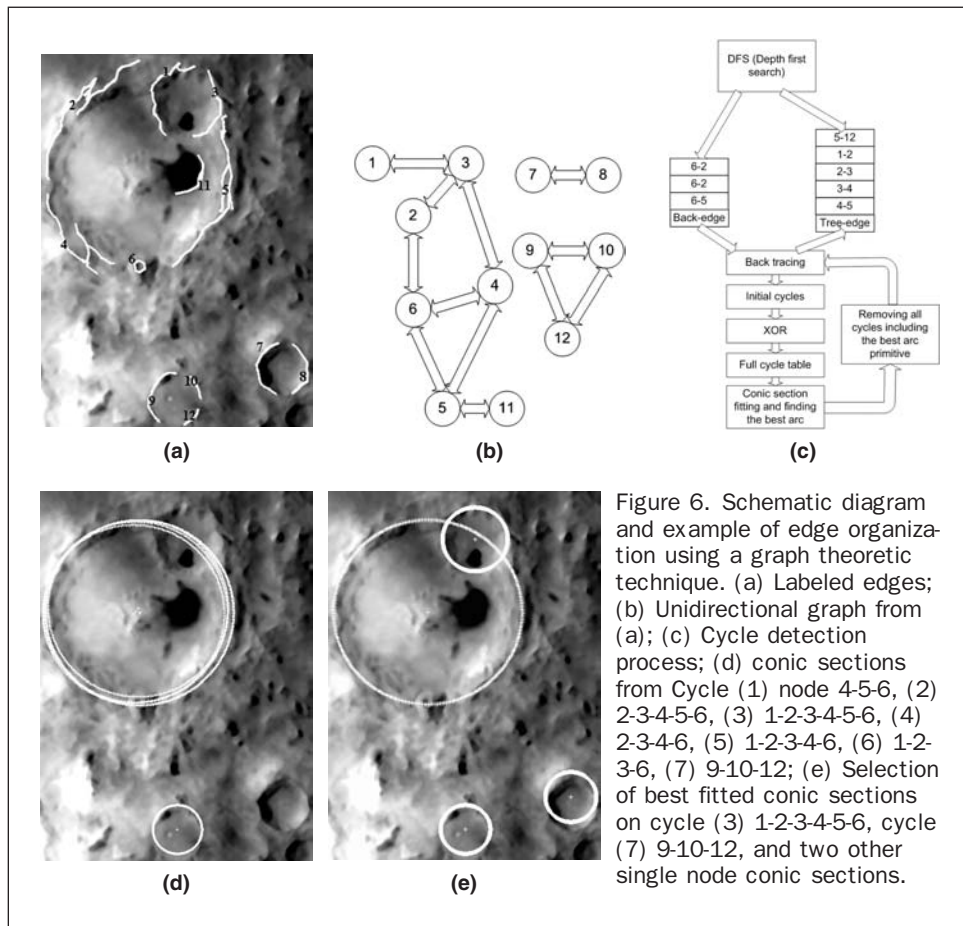

(a) (b) (c)

(d) (e)

Figure 6. Schematic diagram and example of edge organization using a graph theoretic technique. (a) Labeled edges; (b) Unidirectional graph from (a); (c) Cycle detection process; (d) conic sections from Cycle (1) node 4-5-6, (2) 2-3-4-5-6, (3) 1-2-3-4-5-6, (4) 2-3-4-6, (5) 1-2-3-4-6, (6) 1-2-3-6, (7) 9-10-12; (e) Selection of best fitted conic sections on cycle (3) 1-2-3-4-5-6, cycle (7) 9-10-12, and two other single node conic sections.
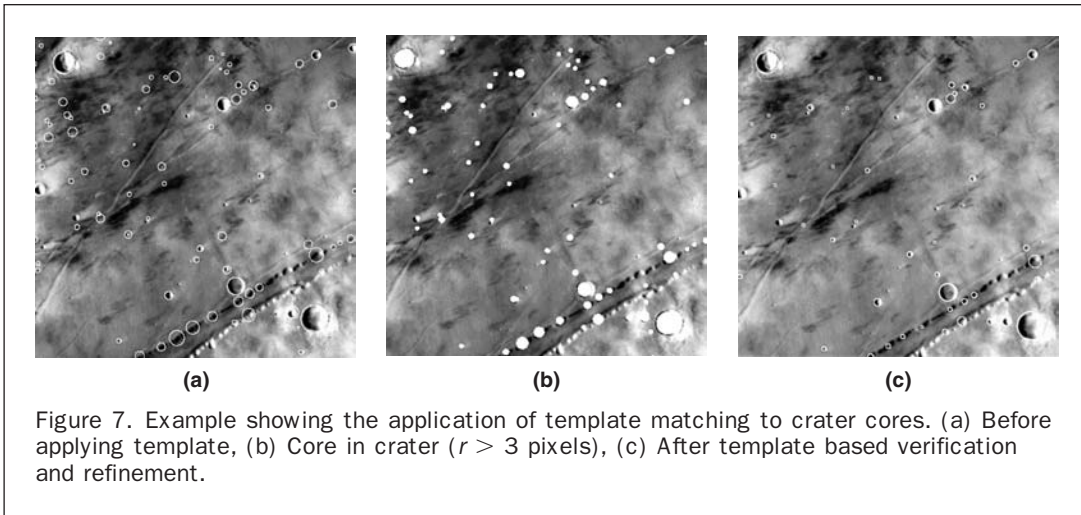
Figure 7. Example showing the application of template matching to crater cores. (a) Before applying template, (b) Core in crater ($r > 3$ pixels), (c) After template based verification and refinement.

of simple template matching. The correlation values and eigenvalues of the Gruen image matcher on the target craters with various sizes and shapes are illustrated in Table 1. The empirical eigenvalue threshold chosen for the Gruen template matching is 150 after resizing the inputs to a radius of 100 pixels to ensure a sufficient numbers of points for template matching of crater targets under any image and illumination conditions. This provides a good solution for verifying large craters. However, the boundary rim refinement is not possible in this case, as with simple template matching method for small craters. Instead of rim refinement, only center point adjustment using shift values from the results of applying the image matcher can be extracted.

False Detection Removal by Eigencrater and Neural Network

One serious drawback of these algorithms is that there could be a large number of false detections which result from crater-like features, such as valleys, shadows, small volcanoes, and scratches (for digitized film products). For these morphologically similar features, correlation values with a template can be much higher than our threshold value of 0.6. To address such problems, we employ the method of eigencrater construction (Turk and Pentland,

TABLE 1. EXAMPLE TEMPLATE MATCHING RESULTS OF CRATER TARGETS TOGETHER WITH VALUES OF THE DERIVED CROSS-CORRELATION AND ADAPTIVE LEAST SQUARES MAXIMUM EIGENVALUES OF THE VARIANCE-COVARIANCE MATRIX

Template	Original image patch	Re-sampled image patch by Gruen process	Eigen-value	Cross-correlation	Verification result
			426	0.86	Reject
			152	0.68	Reject (wrong decision)
			49	0.83	Accept
			171	0.71	Reject
			146	0.72	Accept

1991) and recognition by neural networks, which was originally developed for human face recognition using the following steps which are illustrated in Figure 8.

The main concept behind Turk and Pentland's scheme is the compression of image information into eigenspace from the original image space by:
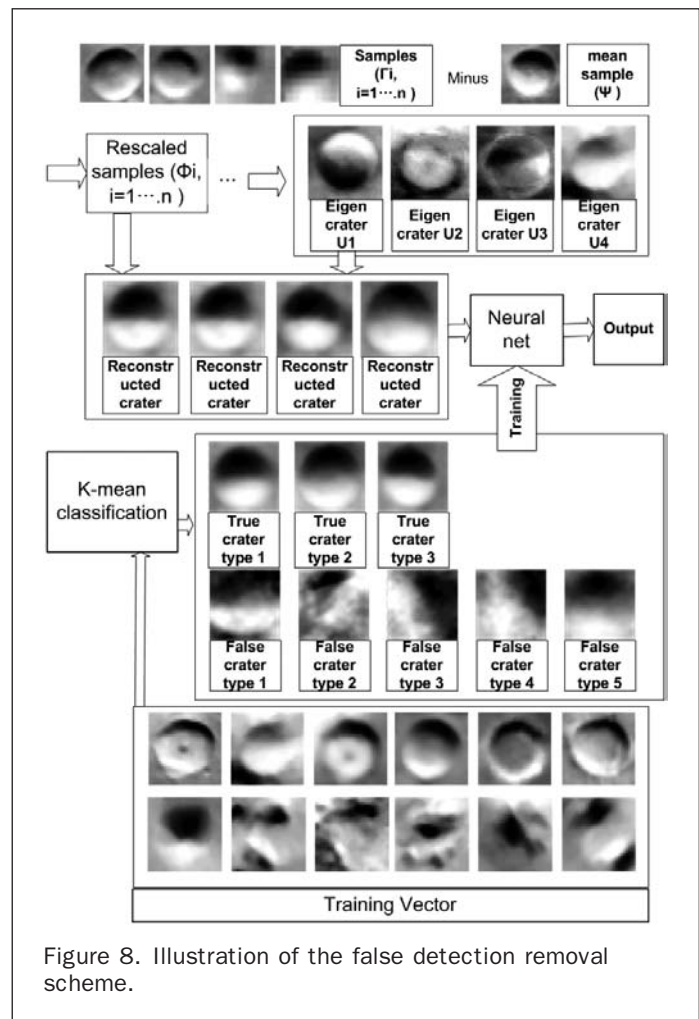

Figure 8. Illustration of the false detection removal scheme.

$$\Phi_i = \Gamma_i - \Psi$$

$$C = \frac{1}{M}\sum_{n=1}^{M}\Phi_n\Phi_n^T = AA^T$$

$$L = AA^T \tag{8}$$

where Γ_i is the ith intensity matrix of a sample crater, Φ_i is the ith intensity matrix of the rescaled crater, Ψ is the intensity matrix of mean crater from the set of Γ_i, C is the covariance matrix, and L is an M × M matrix.

Then, the eigencraters in the new eigenspace can be determined as follows:

$$u_l = \sum_{k=1}^{M}v_{lk}\Phi_k \tag{9}$$

where ν_l is the eigenvector of L (from Equation 10), u_l is the lth eigencrater and M is the desired image dimension, $l = 1, \ldots, M$. (refer to Figure 8 for examples)

These procedures require a transformation from image (row by column) dimension to M dimensional eigenspace. Then, a template can be compared with pre-defined true and false craters using extracted eigencrater components and weight values without the need for pixel-by-pixel comparison. Moreover the recognition scheme becomes robust against noise and the variation of illumination present from one image to the next.

The new image template can be classified by transforming into eigencrater space as follows:

$$\omega_k = u_k^T(\Gamma_{new} - \Psi), k = 1 \ldots M$$
$$\Omega_{new}^T = [\omega_1, \omega_2 \ldots \omega_M] \tag{10}$$

where Γ_{new} is the input crater, ω_k is the weight vector of a new image, and Ω_{new} is the pattern vector of all input craters. Which means that the characteristic of a new template can be compressed into (ω_1, ω_2 . . . ω_M) coefficients, which can be readily processed using a neural network.

After this classification, the next problem addressed is the training vector labeling of crater and non-crater classes. Our approach is similar to Sung and Poggio's (1998) modeling method using a k-means clustering algorithm. Figure 8 shows defined crater and non-crater patterns using eigencraters. In this example, three classes of crater features and four non-crater classes are reconstructed by the automatic detection process without a verification stage, and 121 samples are manually selected. A back propagation neural network was then trained using these labeled training vectors. In a real application with a

number of sample images, it shows a good efficiency (the detection ratio of false craters ≥85 percent, Figure 9). One drawback with this approach is that re-training is usually required for different sensors.

Crater Detection with MOLA DTMS

The output from the detection process based on a high resolution DTM such as MOLA could be required for verification or as a source of complementary data. The detail obtained with this detection process is similar to that of crater detection using optical images. The difference in this DTM crater detection algorithm is as follows: (a) ROIs are defined from high slope areas instead of texture analysis, (b) ridge and channel points (Wood, 2003) are used to substitute edge lines from optical images, and (c) the verification process uses DTM templates. A result is shown in Figure 10b, and assessment is discussed in the next section.

Results and Assessments

The automatic detection methods were applied to various sensors and different geomorphological environments on Mars. These final products have been evaluated by visual inspection, as well as quantitative assessments made through comparisons with the MCC catalogue and manually detected crater ellipses. Finally, an inter-comparison of Size Frequency Distributions (SFDs) is shown for manually derived crater locations with those derived using this algorithm.

Assessment Scheme

For quantitative assessment, quality assessment factors (Shufelt and McKeown, 1993), originally developed for building detection work are introduced as follows:

$$Detection\_Percentage = 100\frac{TP}{TP + FN}$$

$$Branching\_Factor = \frac{FP}{TP}$$

$$Quality\_Percentage = 100\frac{TP}{TP + FP + FN} \tag{11}$$

where True Positive (TP) stands for when both data sets (detected crater and comparison data set) classify the area as being part of a crater, True Negative (TN) when both data sets classify the area as being part of the background, False Positive (FP) when the detected data set classifies the area as a crater, but the comparison data set classifies it as background and False Negative (FN) when the detected data set
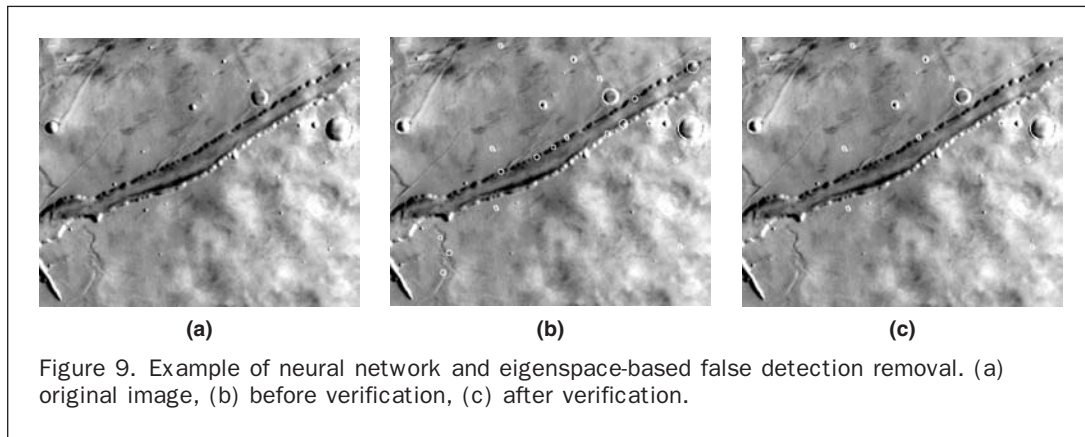

| (a) | (b) | (c) |

Figure 9. Example of neural network and eigenspace-based false detection removal. (a) original image, (b) before verification, (c) after verification.
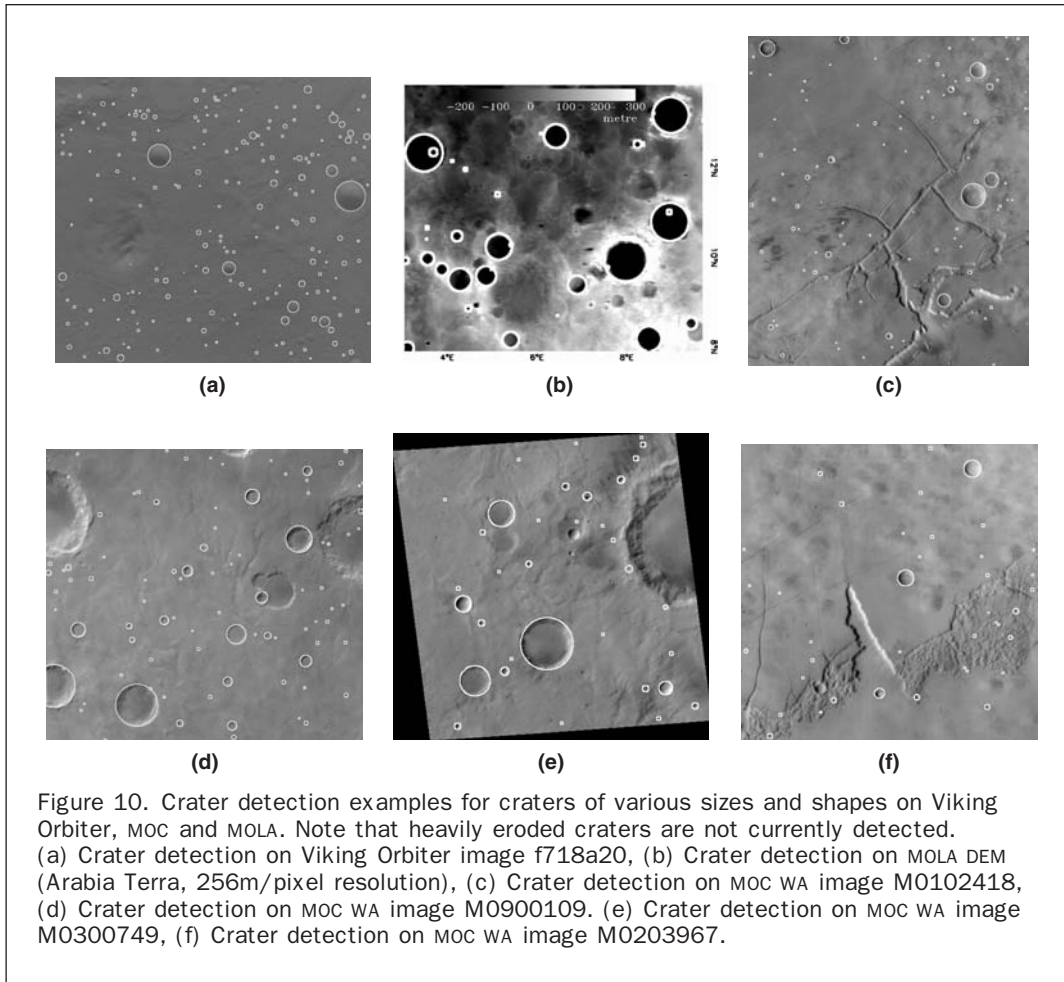
Figure 10. Crater detection examples for craters of various sizes and shapes on Viking Orbiter, MOC and MOLA. Note that heavily eroded craters are not currently detected. (a) Crater detection on Viking Orbiter image f718a20, (b) Crater detection on MOLA DEM (Arabia Terra, 256m/pixel resolution), (c) Crater detection on MOC WA image M0102418, (d) Crater detection on MOC WA image M0900109. (e) Crater detection on MOC WA image M0300749, (f) Crater detection on MOC WA image M0203967.

classifies the area as background while the comparison data set classifies it as a crater.

Detection Results for Sensors

The detection ratio for Viking Orbiter images (Figure 10a), which is tested using a few images, is a little lower (approximately 3 to 4 percent) than for MOC WA images. However, in spite of the low contrast of the VO image, the algorithm works well and satisfactorily detects even shallow craters.

Several examples of crater detection on MOC WA (200 m) and HRSC (12.5 m) images, are shown in Figure 10 and Figure 11. Overall, the detection ratio of relatively small impact craters ($8 < r \leq 60$ pixels) is excellent, but large or multi-ringed structured craters show relatively poor detection accuracy. However, it should be noted that the MCC catalogue, which is complete for diameters ≥ 5 km, already includes information on most, if not all of these larger craters. A quantitative assessment of the detection results on MOC WA images such as those shown in Figure 10c through 10f using the MCC Barlow sets and manually measured data sets are shown in Table 2. Global crater databases at HRSC resolution do not exist, so the assessment of the detection result, which are shown partly in Figure 11 were performed using manual measurements (Table 3).

As seen in Table 2, crater detection on MOC WA images appears to have a very high reliability. We believe that the detection ratio ($8 < r \leq 60$ pixels) is sufficiently high such

that it can be employed as a practical tool. In the small crater size range ($3 \leq r \leq 8$ pixels), quality percentage is lower than the potential critical value for practical applications (about 80 percent; B. Mayer, personal communication, 2004) which is because false detection recognition schemes using neural networks do not appear to work well for craters with small radii.

The HRSC crater detection ratio appears to be considerably lower than for the case of MOC images. The reason for this lower quality percentage is that there appear to be a number of false alarms that were not fully removed. The oblique viewing geometry of HRSC sensors or morphological undulations at fine resolution can result in the distortion of a small crater shape which cannot currently be effectively discriminated against using the current false crater removal scheme, which employs neural networks and eigencraters.

For MOLA DTM-based crater detection, our analysis showed a detection ratio of 73 percent for large craters ($r > 4$ km) compared with manual measurements. Even though craters are detected, the correct radius is frequently not determined. An improved verification method based on some other invariant properties might be a solution and is currently under investigation.

Discussion

It should also be noted that a number of parameter values had to be determined empirically and used to optimize the detection ratios in both the MOC and HRSC imagery. Table 4
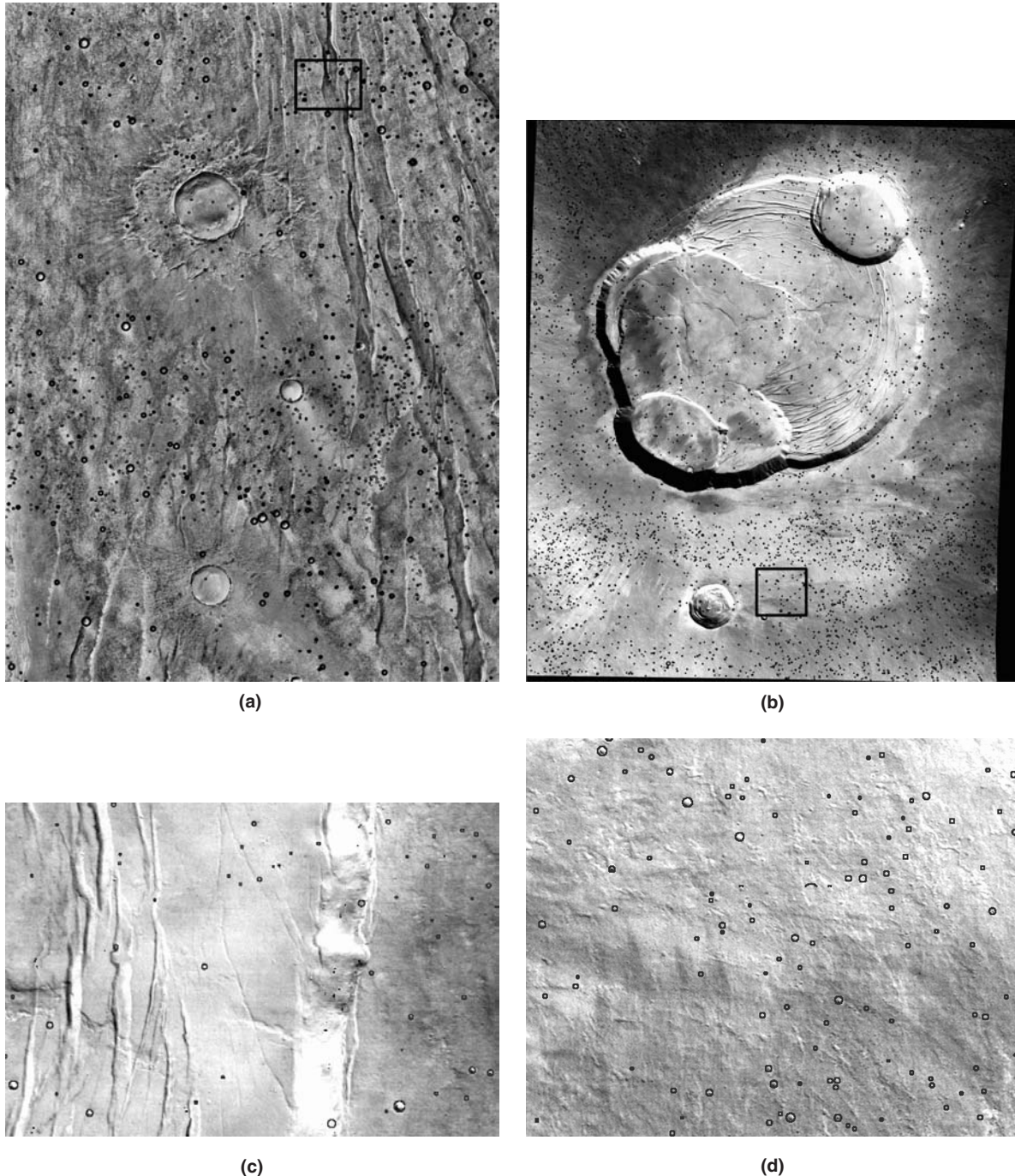
Figure 11. Crater detection results on HRSC images of Claritas Fossae (Orbit 68, 24.3°-21.0° S, 254.9°-259.3° E) and Olympus Mons (Orbit 37, 17.0°-19.1° N, 225.9°-227.8° E). (a) Crater detection result on Claritas Fossae, Orbit 68 nadir image HRSC (6,180 by 8,000 pixel subset, 1,424 craters detected), (b) Crater detection result on Olympus Mons, Orbit 37, HRSC nadir image, (8,927 by 10,094 pixel subset, 3,860 craters are detected), (c) Close-up of Orbit 68 image (715 by 483 pixel size, black box area in (a)), (d) Close-up of Orbit 37 image (606 by 489 pixel size, black box area in (b)).

shows a summary of all these parameters and their typical values. The precise choice of these values is not so crucial for detection accuracy if the false crater removal scheme is working successfully which is because our approach is to detect all possible crater candidates during the focusing and organization stages using generous thresholds, and only to remove false detections at the verification stage. However,

two parameters, the thresholding value of the fitness function and the correlation value at the verification stage, need to be carefully chosen in highly undulating areas or HRSC images as shown in Table 4. Otherwise, false negative detections are increased.

Currently, our algorithm has several drawbacks. First of all, the algorithm appears to fail on very rough and undu-

TABLE 2. IMPACT CRATER DETECTION RATIO FROM AN INTER-COMPARISON WITH MCC AND MANUAL MEASUREMENTS IN 14 RANDOM MOC WA IMAGES SUCH AS THOSE SHOWN IN FIGURE 10 INCLUDING A VERY LARGE RANGE OF DIFFERENT GEOMORPHOLOGICAL TYPES INCLUDING VALLEYS, FRACTURES, ATTACHED CRATERS, UNDULATING AREAS, AND ERODED CRATERS

		Manual Measurements		
	MCC (Barlow)	Small Size	Large Size	Total
True positively detected crater numbers	60	298	80	378
False positively detected crater numbers	*	45	7	52
False negatively detected crater numbers	11	42	11	53
Detection percentage	85%	87.6%	87.9%	87.7%
Branching factor	—	0.15	0.09	0.15
Quality percentage	—	77.4%	81.6%	78.3%

Small size: R ≤ 8 pixels, Large Size: 8 < R ≤ 60 pixels
*False positive has no meaning for the MCC inter-comparison, because MCC data sets do not aim to catalogue all craters in a target area. Also, true negative has no meaning for individual crater detection.

lating areas, as seen in Figure 12a, because these include many false crater detections, and the neural network-based verification method is not reliable enough to remove the majority of false alarms. Additionally, composite impact craters are frequently mis-detected. As yet, we have no solution for this, because there are few image clues to split connected edges, as illustrated in Figure 12b. Also, there are many images which are noisy or hazy; manual exclusion of those images is currently necessary.

Even though all the algorithms appear to work well, some erroneous detection results are inevitable. We are therefore developing a cross-verification process between detections from optical images, i.e., overlapping MOC images or HRSC stereo pairs, and/or DTMs, to generate more extensive and reliable crater maps. This process should be operational in the near future if an automated co-registration procedure using bundle block adjustment between optical images and DTMs, such as MOLA can be implemented.

Example Application: Crater SFD Analysis for Surface Age Dating

The locations and physical characteristics (such as radii) of all the craters automatically detected in the volcanic caldera of Olympus Mons (see Figure 11c) were used to produce a crater Size-Frequency Distribution (SFD) for different geological units (see Figure 13a, taken from Neukum *et al.*, 2004). The SFDs derived from manual measurements kindly pro-

TABLE 4. DETAILS OF FACTORS EMPLOYED IN THE CRATER DETECTION ALGORITHM

Factor	Description	Typical Value	Remarks
d_{max}	Distance parameter from RoI boundary	Depends on the size of GLCM window	≈ GLCM window
θ_t	Threshold value of the interior angle between an edge pair to form an edge primitive	135 degrees	
Op_{th}	Threshold value of overlap in first fitted conic section	Usually 0.5	
Ecc_{th}	Threshold value of eccentricity	Depends on the latitude and aspect ratio of image	
Fit_{th}	Threshold value of fitness	Empirically 0.15–0.25 in equation (6) and 0.3 in equation (7) For final fitted conic section usually 0.4	Needs to be decreased in noisy or undulated images to 30–40 percent lower values
$Corr_{th}$	Threshold value of correlation with template and crater candidates	Usually 0.6	In undulating MOC or HRSC image, usually low (≈0.4)
n_s	Size of structuring element in fitness function	$max(const*r,1.0)$ in pixel const = 0.1–0.2, r is the radius of fitted conic	

vided by Stephanie Werner (Free University Berlin) are plotted alongside results from the automated method (indicated as KM here) in Figure 13b and c, respectively. When comparing the manually derived crater SFDs with the automatically detected distribution using the KM method two major differences become apparent: (a) The KM method showed significant differences for craters with smaller diameters down to 30 meters compared with the manual method, and (b) the cumulative distribution derived by the automatic detection method shows the characteristic bend at small-diameters significantly earlier than the manually derived distribution. Both characteristics appear to be caused by a lower percentage of HRSC detection results for smaller craters due perhaps to the ineffective false crater removal scheme as previously described. Additionally, not

TABLE 3. IMPACT CRATER DETECTION RATIO ASSESSMENTS ON HRSC IMAGE WITH MANUAL MEASUREMENT IN TWO SAMPLE AREAS

	High Undulating Area (part of Orbit 37)			Low Undulating Area (part of Orbit 68)		
	Small Size	Large Size	Total	Small Size	Large Size	Total
True positively detected crater number	119	6	125	60	16	76
False positively detected crater number	20	1	21	15	4	19
False negatively detected crater number	52	2	54	7	3	10
Detection percentage	69.6%	75%	69.8%	89%	84.2%	88.3%
Branching factor	0.17	0.17	0.17	0.25	0.25	0.25
Quality percentage	62.3%	67%	62.5%	73.1%	69.5%	72.3%

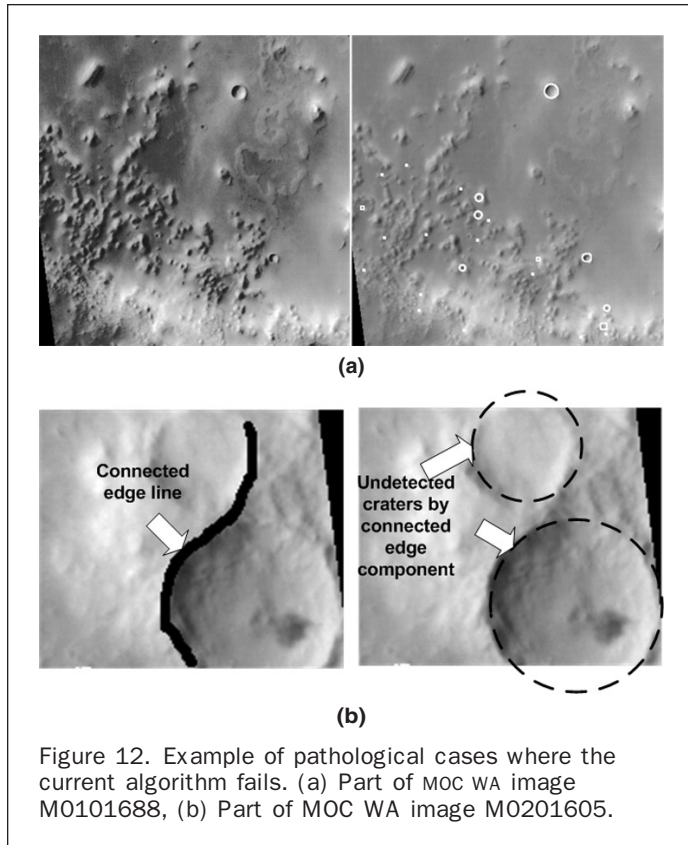Small size: R ≤ 8 pixels, Large Size: 8 < R ≤ 60 pixels.

Figure 12. Example of pathological cases where the current algorithm fails. (a) Part of MOC WA image M0101688, (b) Part of MOC WA image M0201605.

all craters between 200 m and 700 m in diameters were detected. The deviation in the larger diameter range may be caused by the partial erosion of crater rims and the superposition of target craters.

Appropriate image pre-processing and a cross verification process between the detection results from optical images, for example HRSC stereo pairs, may be able to correct automatically derived distributions in future. Kim (2005) provides some examples of a "crater pair" detection algorithm for any interested reader, although it should be noted that the detailed part of the algorithm needs to be updated for effective detection of all crater pairs (with diameters from 200 m to 700 m) for a better SFD extraction using HRSC stereo pairs. The underestimation of SFD for smaller craters (<200 m) means that currently, the automatic crater detection method can be employed for age dating but should exclude craters in the 30 m to 200 m size range.

The discussion about derived ages is another matter: interpretation of surface ages has always to be based upon (the subjective) geologic mapping of the area which is expected to be emplaced during a single event (e.g., Hartmann, 2005). Any resurfacing event would be apparent in the SFD and re-mapping has to be considered. For the determination of relative ages despite any systematic error in the automatic detection, the results will always allow the derivation of a sequence of events. Of course, exhumation, secondary cratering, and resurfacing can obscure the results.

The definition of the appropriate crater production function has been subject to discussion for over 30 years and has been recently reactivated with the investigation of the Zunil impact and its secondary craters (McEwen *et al.*, 2005). These researchers argue that small (≤200 m) craters are unsuitable for age dating; if so, the poor detection of such craters by the KM method would be less significant.

This conclusion is not universally accepted, however; the choice to use a polynomial expression by Neukum (1983), refined by Ivanov (2001), was utilized for reasons of simplicity and to facilitate comparison of surface ages derived from our crater counts with those derived under the same assumptions from the manual measurements by Neukum *et al.* (2004), who consider the smallest craters to be useful for dating. The KM-derived ages shown in Figure 13c range from 70 to 90 percent of the equivalent manually derived values shown in Figure 13a.

In the current procedure, relative (and derived absolute) age determinations may be biased if craters of a particular crater size range are underestimated due to limitations in the algorithm, and this size range is not excluded from the age calculation. This implies that further work is required to improve the detection efficiency of the KM method and that currently manual methods may still be required to maximize the fraction of visible craters that are included in counts. Our results may ultimately allow differing theories of crater counting and the role of secondary cratering to be tested more rigorously, once a suitably improved KM algorithm can be applied to very large areas to generate extensive statistics.

Conclusions

Automated impact crater detection algorithms have been developed to identify various sizes of impact craters under different conditions such as illumination and view angles and geographical complexity. The algorithm described here exhibits a detection accuracy, when compared against manual measurements (MCC catalogue and selected measurements), from a minimum 70 percent detection ratio for small size craters (<8 pixels) in highly undulating HRSC images to 87 percent in MOC WA images under a large variety of different conditions. In general, we believe that the current overall approach, consisting of three stages of focusing, organization and verification, shows great potential for future application to very large areas to provide extensive crater databases and automated age mapping. These capabilities are especially relevant with the release of new high resolution Mars optical images such as HRSC. However, certain detailed aspects of the algorithms require improvement as well as extensions both into the exploitation of high resolution DTMs now possible from HRSC (Albertz *et al.* 2005; Scholten *et al.*, 2005), as well as cross verification between co-registered optical images.

References

Albertz, J., M. Attwenger, J. Barrett, S. Casley, P. Dorninger, E. Dorrer, H. Ebner, S. Gehrke, B. Giese, K. Gwinner, C. Heipke, E. Howington-Kraus, R.L. Kirk, H. Lehmann, H. Mayer, J-P. Muller, J. Oberst, A. Ostrovskiy, J. Renter, S. Reznik, R. Schmidt, F. Scholten, M. Spiegel, U. Stilla, M. Wählisch, G. Neukum and the HRSC Col-Team, 2005. HRSC on Mars Express – Photogrammetric and Cartographic Research, *Photogrammetric Engineering & Remote Sensing*, 71 (10).

Barlow, N.G., 2003. Revision of the catalog of large Martian impact craters, *International Conference on Mars*, 20–25 July, Pasadena, California, URL: *http://www.lpi.usra.edu/meetings/sixthmars2003/pdf/3073.pdf* (last date accessed: 15 July 2005).
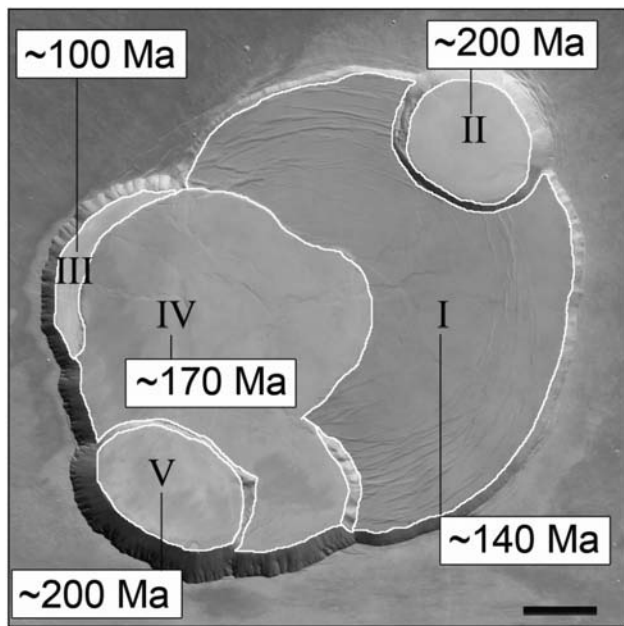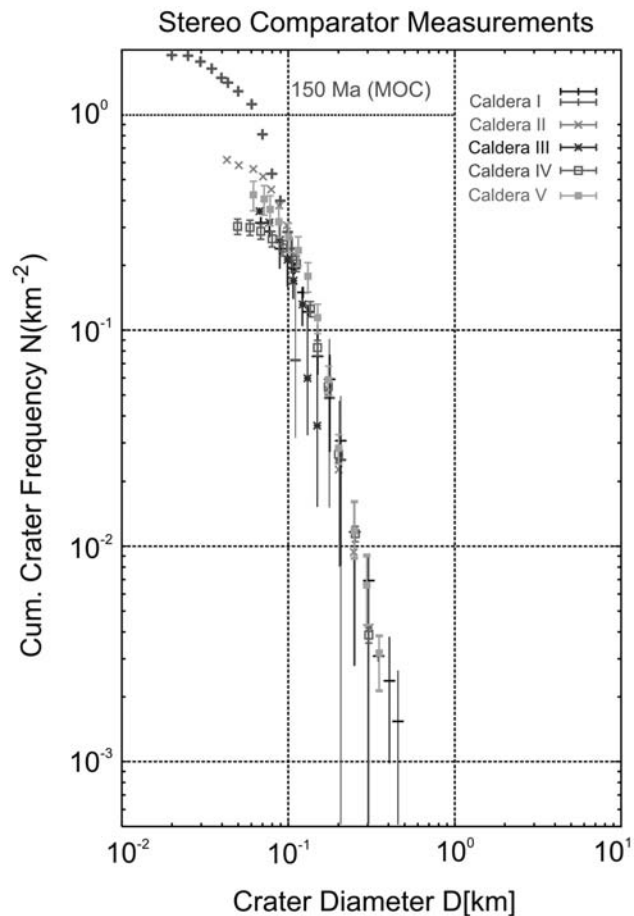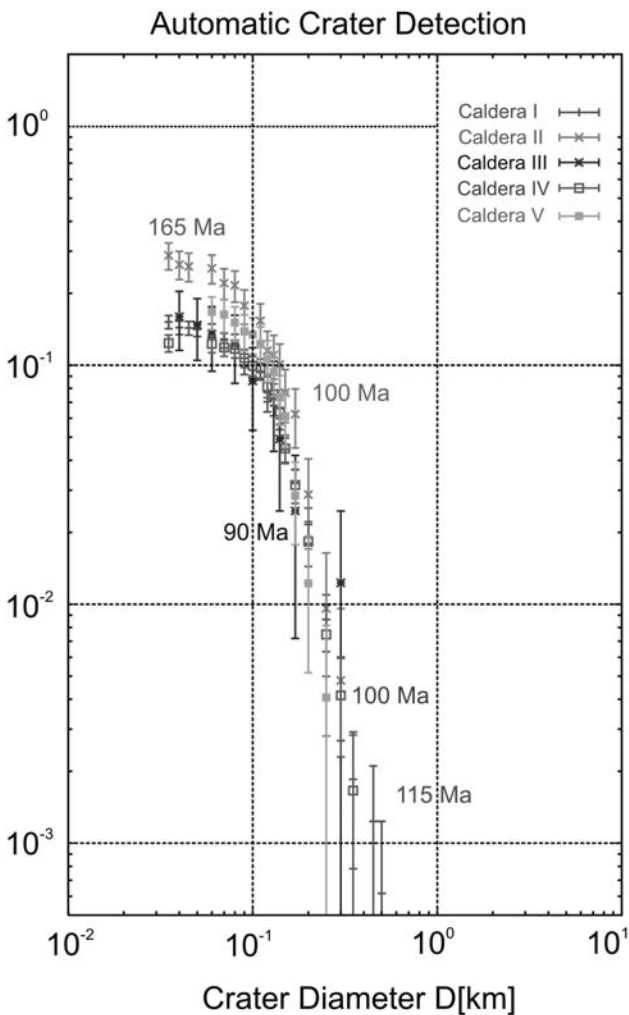
(a)

Figure 13. Demonstration of the automated method for SFDS extraction compared against the SFDS derived using manual measurements. (a) Areas of different geological type and age segmented by hand, (b) SFD derived from manual measurements, (c) SFD derived automatically using the KM methods.

Bottke, W.F., S.G. Love, D. Tytell, and T. Glotch, 2000. Interpreting the elliptical crater populations on Mars, Venus, and Moon, *Icarus*, 145(1):108–121.

Cheng, Y., A.E. Johnson, L.H. Matthies, and C.F. Olsen, 2003. Optical landmark detection for spacecraft navigation, *Proceedings of the 13th AAS/AIAA Space Flight Mechanics Meeting*, Ponce, Puerto Rico, February, AAS 03–235.

Fitzgibbon, A., M. Pilu, and R. Fisher, 1999. Direct least square fitting of ellipses, *IEEE Transactions on Pattern Analysis and Machine Intelligence*, 21(5):476–480.

Forsberg-Taylor, N., A.D. Howard, and R. Craddock, 2004. Crater degradation in the Martian highland: Morphometric analysis of the Sinus Sabaeus region and simulation modeling suggest fluvial process, *Journal of Geophysical Research*, 109, E05002 (doi:10.1029/2004JE002242).

Gruen, A.W., 1985. Adaptive least squares correlation: A powerful image matching technique, *South African Journal of Photogrammetry Remote Sensing and Cartography*, 13(3):175–187.

Haralick, R.M., 1979. Statistical and structural approaches to texture, *Proceedings of the IEEE*, 67(5):786–804.

Hartmann, W.K., 2005. Martian cratering 8: Isochron refinement and the chronology of Mars, *Icarus*, 174(2):294–320.

Huang, C.T., and O.R. Mitchell, 1994. A Euclidean distance transformation using grayscale morphology decomposition, *IEEE Transactions on Pattern Analysis and Machine Intelligence*, 16(4):443–448.

Honda, R., Y. Iijima, and O. Konishi, 2002. Mining of topographic feature from heterogeneous imagery and its application to lunar craters, *Proceeding of the Progress of Discovery Science*, Berlin, LNAI 2281:395–407.

Ivanov, B., 2001. Mars/Moon cratering rate ratio estimates, *Chronology and Evolution of Mars*, (R. Kallenbach, J. Geiss, and W.K. Hartmann, editors), International Space Science Institute, Bern, pp. 87–104.

Kanazawa, Y., and K. Kannatani, 1996. Optimal conic fitting and reliability evaluation, *Institute of Electronics, Information and Communication Engineering, Transactions on Information and Systems*, E79-D(9):1323–1328.

Kim, H.S., and J.H. Kim, 2001. Two step circle detection algorithm from the intersection chords, *Pattern Recognition Letter*, 22(6):787–798.

Kim, J.R., 2005. *Landscape Object Detection and Reconstruction Using Multi-sensor Data Fusion*, PhD. thesis, (unpublished), University of London, 409 p.

Kim, J.R., and J-P. Muller, 2003. Impact crater detection on optical image and DEM, *ISPRS WG IV/9: Extraterrestrial Mapping Workshop "Advances in Planetary Mapping 2003"*, 22 March, Houston, Texas, URL: http://astrogeology.usgs.gov/Projects/ISPRS/MEETINGS/Houston2003/index_houston.html (last date accessed: 15 July 2005).

Kim, J.R., J-P. Muller, and J.G. Morley, 2004. Quality assessment of automated crater detection on Mars, *XXth ISPRS Congress*, 12–23 July, Istanbul, Turkey, unpaginated CD-ROM.

Kirk, R.L., E. Howington-Kraus, B. Redding, D. Galuszka, T.M. Hare, B.A. Archinal, L.A. Soderblom, and J.M. Barrett, 2003. High-resolution topomapping of candidate MER landing sites with Mars Orbiter Camera Narrow-Angle images, *Journal of Geophysical Research*, 108, E12 (doi: 10.1029/2003JE002131).

Kuzmin, R.O., R. Greeley, S.C. Rafkin, and R. Haberle, 2001. Wind-related modification of some small impact craters on Mars, *Icarus*, 153(1):61–70.

Leroy, B., G.G. Medioni, E. Johnson, and L. Matthies, 2001. Crater detection for autonomous landing on asteroids, *Image and Vision Computing*, 19(11):787–792.

Magee, M., C.R. Chapman, S.W. Dellenback, B. Enke, W.J. Merline, and M.P. Rigney, 2003. Automated identification of martian craters using image processing, *Lunar and Planetary Science Conference*, 17–21 March, Houston, Texas, unpaginated CD-ROM.

McEwen, A.S., B.S. Preblich, E.P. Turtle, N.A. Artemieva, M.P. Golombek, M. Hurst, R.L. Kirk, D.M. Burr, and P.R. Christensen, 2005. The rayed crater Zunil and interpretations of small impact craters on Mars, *Icarus*, 176(2):351–381.

Neukum, G., 1983. *Meteoritenbombardment und Datierung Planetarer Oberflachen*, Thesis, Ludwig-Maximillians-University, Munich, 186 p.

Neukum, G., R. Jaumann, H. Hoffmann, E. Hauber, J.W. Head, A.T. Basilevsky, B.A. Ivanov, S.C. Werner, S. Van Gasselt, J.B. Murray, T. Mccord, and The HRSC Co-investigator Team, 2004. Recent and episodic volcanic and glacial activity on Mars revealed by the High Resolution Stereo Camera, *Nature*, 432:972–979

Olson, C.F., 1999. Constrained Hough transformations for curve detection, *Computer and Image Understanding*, 27(3):329–345.

Scholten, F., K. Gwinner, T. Roatsch, K.-D. Matz, M. Wählisch, B. Giese, J. Oberst, R. Jaumann, and G. Neukum, 2005. Mars Express HRSC data processing – Methods and operational aspects, *Photogrammetric Engineering & Remote Sensing*, 71 (10).

Shufelt, J., and D.M. McKeown, 1993. Fusion of monocular cues to detect man-made structures in aerial imagery, *Computer Vision and Image Understanding*, 57(3):307–330.

Sung, K., and T. Poggio, 1998. Example-based learning for view-based human face detection, *IEEE Transactions on Pattern Analysis and Machine Intelligence*, 20(1):39–50.

Thomas, S.M., and Y.T. Chan, 1989. A simple approach for the estimation of circular arc center and its radius, *Image Vision, Graphic and Image Processing*, 45(2):362–370.

Turk, M., and A. Pentland, 1991. Eigenfaces for recognition, *Journal of Cognitive Neuroscience*, 3(1):71–86.

Vinogradova, T., M. Burl, and E. Mjolsness, 2002. Training of a crater detection algorithm for Mars crater imagery, *Proceeding of the IEEE Aerospace Conference*, 09–16 March, Big-Sky, Montana, (7):7-3201–7-3211.

Wood, J., 1996. The *Geomorphological Characterization of Digital Elevation Models*, Ph.D. Dissertation, the Department of Geography, University of Leicester, Leicester, pp. 80–110.

Yuen, H.K., J. Illingworth, and J.V. Kittler, 1989. Detecting partially occluded ellipses using the Hough transform, *Image and Vision Computing*, 7(1):31–37.